Tectonophysics 560–561 (2012) 94–104

Contents lists available at SciVerse ScienceDirect

Tectonophysics

journal homepage: www.elsevier.com/locate/tecto

Practical implications of the geometrical sensitivity of elastic dislocation models for field geologic surveys

Ravi V.S. Kanda *, Mark Simons

Seismological Laboratory, California Institute of Technology, 1200 E. California Blvd., MC 252-21, Pasadena, CA 91125, USA

ARTICLE INFO

Article history:
Received 27 November 2011
Received in revised form 15 May 2012
Accepted 20 June 2012
Available online 4 July 2012

Keywords:
Subduction zone seismic cycle deformation
Sensitivity to plate geometry and slip distribution
Coastal uplift and hingeline
Elastic subducting plate model
Backslip model
Geodetic data inversion

ABSTRACT

Geodetic observations of both coseismic and interseismic surface deformation fields in the vicinity of subduction zones are frequently interpreted using simple elastic dislocation models (EDMs). The geometry of the megathrust interface used in these models has a first order effect on their predicted surface deformation. Here, we systematically explore the sensitivity of the surface velocity field predicted by EDMs both early and late in the seismic cycle, to parameterizations of megathrust interface geometry, effective subducting plate thickness, and gradual transitions in apparent plate coupling. We focus on how these parameterizations affect the hingeline – the location where vertical velocities switch from subsidence to uplift – as well as the location of the peak uplift rates. We find that these surface observables are much less sensitive to uncertainties in dip at the downdip end of the seismogenic zone for realistic curved faults in comparison to planar faults. For realistic megathrust geometries (planar or curved) having gradual transitions in apparent plate coupling, we find that the extent of locking is best approximated at the surface by the location of peak uplift rates. Therefore, the common notion – based on shallow-dipping planar faults – that the hingeline is located directly above the maximum depth extent of the locked plate interface is generally incorrect. Using the hingeline as the basis for coupling may lead to a significant underestimation of seismic hazard early in the cycle, as well as during the interseismic period. This analysis also demonstrates the importance of considering both vertical and horizontal velocities for determining seismic source extents, as well as interseismic coupling, on the megathrust. The tradeoffs presented here between the geometry of the megathrust and fault coupling along its surface can assist in the planning of campaign-GPS or field geologic surveys, and help improve seismic hazard estimates in active subduction zones.

1. Introduction

At subduction plate boundaries, geodetic data from the interseismic period – decades to centuries after a megathrust earthquake – help to delineate regions of the megathrust that are not presently slipping (i.e., apparently coupled) and can potentially produce large earthquakes. Similarly, field geologic surveys of coastal uplift and subsidence in the weeks to months following an earthquake (as well as geodetic data, where available) can help delineate the extent of its rupture area on the megathrust. Due to observational, theoretical, and computational considerations, such data are frequently interpreted using elastic dislocations embedded in the halfspace (henceforth referred to as elastic dislocation models, or EDMs). The simplest of these EDMs, the backslip model (the BSM, see Savage, 1983), has been widely used in modeling interseismic period geodetic data in subduction zones (e.g., Khazaradze and Klotz, 2003; Savage, 1995; Suwa et al., 2006; Wang et al., 2003; Zweck et al., 2002). The BSM can essentially be described with only a few parameters — the extent and distribution of the apparently locked areas along the fault interface, and the fault geometry. The BSM is motivated by the recognition that for mature subduction zones, the over-riding plate experiences little permanent inelastic deformation on time scales relevant to the seismic cycle (less than a few thousand years) (see Savage, 1983; Wang and Hu, 2006). Thus, to first order, the interseismic deformation field late in the seismic-cycle must cancel the sum of the coseismic and postseismic deformation fields (Savage, 1983, 1995).

In a previous study, we demonstrated that the BSM is an end-member case of a more realistic elastic subducting plate model (the ESPM, Kanda and Simons (2010)). We showed that the BSM is equivalent to: (a) an ESPM having 'zero' plate thickness; or (b) an ESPM of finite elastic thickness, in which plate bending stresses are continually being released — either aseismically, or episodically at great depths (>100 km). We also demonstrated that the BSM would fit available geodetic data as accurately as the ESPM, owing to the spatial distribution of current geodetic networks (i.e., starting at a distance of 100–200 km landward of the trench). The assumption

* Corresponding author at: Dept. of Geological Sciences, National Taiwan University, No. 1, Sec. 4, Roosevelt Rd, Taipei, 10617, Taiwan, ROC. Tel.: +886 2 2363 6450x214; fax: +886 2 2364 4625.
E-mail addresses: rkanda@alumni.caltech.edu (R.V.S. Kanda), simons@gps.caltech.edu (M. Simons).

0040-1951/$ – see front matter © 2012 Elsevier B.V. All rights reserved.
doi:10.1016/j.tecto.2012.06.040

of an elastic halfspace has also been relaxed (e.g., Savage, 1998), but surface velocity fields predicted by layered EDMs (as well as their spatial gradients) are not significantly different from those for the homogeneous halfspace. Including the significant contrast in material properties between the subducting and overriding plates results in a stiffer system that overpredicts horizontal velocities near the trench by 20–25%, compared to homogeneous elastic half-space models (assuming identical fault slip distributions: e.g., Hsu et al., 2011; Masterlark et al., 2001). However, as illustrated in these papers, this overestimation diminishes rapidly towards the coastline. Most significantly, these material property contrasts have only a negligible effect on the predicted vertical velocities (e.g., Fig. 5 of Hsu et al., 2011) and associated surface observables that form the basis of our sensitivity analysis. Therefore, owing to their simplicity as well as success in fitting current geodetic observations, the analysis presented here is entirely based on EDMs in a homogeneous halfspace.

The hingeline associated with coseismic rupture – the location where vertical displacements switch from uplift to subsidence at the surface – is typically estimated from field geologic surveys or campaign-GPS observations immediately following a megathrust earthquake. This coseismic hingeline is frequently interpreted using simple EDMs to infer the extent of coseismic-rupture over the megathrust (or downdip end of the locked-zone). Such rupture extents have been used to estimate: (i) future hazard for local coastal communities in potential megathrust rupture areas (e.g., Meltzner et al. (2006), Natawidjaja (2003), Subarya et al. (2006), Taylor et al. (2008)); (ii) the contribution of megathrust earthquakes to long-term coastal uplifts (e.g., Biggs et al. (2007), Delouis et al. (1998), Ortlieb et al. (1996), Vargas et al. (2011)); and (iii) repeated deposition of organic matter over multiple seismic cycles, which is of practical interest in the petroleum industry (e.g., Dorobek, 2008). The hingeline during the interseismic period – the location where vertical velocities switch from subsidence to uplift at the surface – is typically estimated from geodetic data late in the seismic-cycle. This interseismic hingeline is also often interpreted using simple EDMs to infer regions of slip-deficit (apparent locking) on the megathrust (e.g., Suwa et al., 2006). However, with the recent explosion in the spatio-temporal coverage of geodetic data, more sophisticated dislocation models have been used in geodetically constrained inversions of both coseismic and postseismic slip (e.g., Biggs et al., 2007; Chen et al., 2009; Hsu et al., 2006; Miyazaki et al., 2004; Simons et al., 2011), as well as modeling of slip evolution on fault surfaces (e.g., Hetland and Simons, 2010). 3D slip inversions show that coseismic rupture sources ('asperities') are frequently compact (e.g., Briggs et al., 2006; Koketsu et al., 2004; Sladen et al., 2009), and seem to be surrounded by transition zones that undergo afterslip in the early part of the seismic cycle following a rupture (e.g., Biggs et al., 2007; Chen et al., 2009; Hsu et al., 2006; Miyazaki et al., 2004). Thus, regions on the fault surface that have undergone afterslip appear to occupy a diffuse region (the 'stress-shadow' region) around ruptured asperities. These regions do not undergo significant slip late in the seismic cycle, and are apparently locked during the interseismic period. However, the above analyses do not consider the strong tradeoff between the assumed fault geometry and inferred slip distribution.

In this paper, we want to understand how the hingeline, as well as other key features of the surface deformation field, are influenced by fault geometry and the assumed slip distribution. We systematically explore the sensitivity of the predicted surface deformation field to parameters of the ESPM and the BSM: subduction thrust geometry, the extent of the locked zone, width of the slip-transition zone (which approximates the integrated effects of afterslip and anelastic deformation downdip of the locked zone), and the plate thickness. In particular, we focus on the key characteristics ("observables") of the vertical component of the interseismic velocity (or coseismic displacement) field: locations of the hinge-line, and the location of maximum uplift rate (or maximum subsidence). We approximate the diffuse interseismic 'stress-shadow' regions discussed above by a transitional zone around locked asperities, within which the slip-rate increases from zero (at the inner, asperity edge) to the full plate convergence rate (at the outer edge). Thus, during the interseismic period, the apparent locked zone may include regions on the megathrust that slipped during the coseismic as well as the postseismic periods. The slip-transition zone surrounding a historic asperity represents a conditionally stable region that may rupture coseismically during future, "mega"-events spanning multiple asperities [such as the 2011, M9 Tohoku-oki (Japan) earthquake (e.g., Simons et al., 2011)].

While our analysis focuses on the interseismic velocity field, our results can be directly applied to the co- and post-seismic displacement fields for the following reasons. If we assume zero net deformation of the over-riding plate over the seismic-cycle (as in the BSM), the combined co- and post-seismic (or "early-cycle") surface deformation must equal the interseismic (or "late-cycle") deformation. Therefore, the locations of surface observables for the late-cycle velocity field are identical to those for the early-cycle displacement field — except that the location of maximum late-cycle uplift rate corresponds to that for maximum early-cycle subsidence. In the intuition building "toy" models described here, we only focus on cross-sectional variations in fault geometry and coupling. The 2D analysis presented here allows us to build intuition about the first-order effects of megathrust geometry, without adding additional 3D complexity (e.g., along strike variations) to the problem — i.e., as a first order exploration of the deformation fields at different stages of the seismic cycle.

2. Methodology

For computing surface velocity profiles, we use the 2-D elastic dislocation solutions for a dip-slip fault embedded in an elastic half-space given by Freund and Barnett (1976), as corrected by Rani and Singh (1992) (see also, Tomar and Dhiman (2003) and Cohen (1999)). For simplicity, we assume that the backslip velocity vector, V_b, is uniform and constant over the locked zone, and varies linearly as a function of arc-length over the slip transition zones immediately updip and/or downdip of the asperity. For each profile, we assume that the origin is at the trench, the x-axis is positive landward of the trench, and the z-axis is positive upwards (so depths within the half-space are negative). Dips are positive clockwise from the positive x-axis. Uplift is considered positive for the vertical component of the surface velocity field, and landward motion is considered positive for the horizontal component. The Notation section at the end of this paper contains an explanation of the variables used in our analysis.

Here, we consider planar faults as well as simply parameterized curved fault geometries (a constant curvature arc, or a parabolic profile with decreasing down-dip curvature) passing through the origin (the trench). Further, we assume nearly zero dip at the trench for curved faults. We also consider faults with a single kink (because of their common usage as well as simplicity) and find that their surface velocity predictions can be related to equivalent planar faults. For planar faults, it is straightforward to relate s_{lock} for an asperity to either the depth of its downdip edge, D_{lock}, or the horizontal distance from the trench to the surface projection of this downdip limit, x_{lock}. The simple parameterizations used to generate curved faults result in their arc-length, s, being proportional to their surface projections, x. In addition, our assumption that the bottom-most segment of curved faults (i.e., beyond the fully locked section) is a semi-infinite tangential segment (e.g., top panels of Fig. 2a–d) results in $x_{\max}$ and x_{hinge} being strongly influenced by its dip (e.g., compare profiles of fault-F and fault-d in Fig. 3a; also see discussion in the next section). This assumption of a linear bottom segment is reasonable because as will be seen in the next section, any curvature downdip of the locked zone does not impact surface deformation profiles over an individual seismic cycle (either during the coseismic or the interseismic periods). Since a larger downdip extent (or arc-length) for the fully locked

region of the curved fault, s_{lock}, leads to a steeper dip for this semi-infinite segment, this dip is taken as the characteristic dip of a non-planar fault for comparison with planar faults. Therefore, x_{hinge}, x_{lock} and $x_{\max}$ for curved faults are also implicitly "proportional" to s_{lock}. We approximate these curved faults by a number of discrete ("infinitesimal") tangential line-segments. The predictions for curved faults are thus a superposition of the solutions for a sufficiently large number of tangential edge-dislocations, each corresponding to the local dip and depth of the true fault interface. The superposed curved fault solutions converge rapidly with increasing number of segments. However, in order to minimize the size of regions experiencing singular strain-rates due to segment slope discontinuities ("kinks"), a finer discretization is required. For typical fault curvatures used here, we found that 100 segments were sufficient to restrict such singularities to within a few hundred meters of the kinks.

We also tested the effect of finite along-strike width of the locked asperity, W, using the elastic dislocation solutions presented in Okada (1992). We compared the 2D (or "infinite width") surface velocity predictions with those for asperities with W between one and ten times their along-dip extents, s_{lock} (i.e., aspect ratio, $F_{asp} = W/s_{lock} =$ 1 to 10). We found that the trench-perpendicular velocity profiles (and corresponding strain-rates) along transects across the centers of these asperities were nearly indistinguishable from the 2D solutions for $F_{asp} > 3$. Also, peak uplift rates along these profiles were significantly smaller only for asperities with $F_{asp} < 3$, and that too, for only steeply dipping faults ($>45°$, for which peak uplift rates were smaller by over 50%). For F_{asp} equal to 1, the hingeline shifts landward by less than 5% for shallow dipping faults (dip $<15°$) and 20% or more for very steep faults (dip $>45°$). This shift is nonlinear with respect to fault dip, and is much more pronounced for steep faults. The nonlinear relationship results in a narrowing of the range of fault dips over which the hingeline can be used as a proxy for fault locking extent (see Section 4 for a discussion of these fault dip ranges). This narrower range further strengthens our conclusion that other observables (e.g., location of peak uplift-rate) are more appropriate for estimating the size of the locked zone. As F_{asp} increases from 1 to 3, these hingeline shifts are reduced by as much as 50% over the entire range of dips considered. So, except when $F_{asp} \leq 1$, and/or an asperity is located along a steeply dipping fault interface, the 2D profiles of slip and surface velocity presented here are a good approximation of trench-perpendicular cross-sections of the respective 3D fields predicted for a realistic (finite-width) asperity, along a transect passing over its center.

The 2D cross-sectional analysis here can be easily extended to real 3D megathrust interfaces, with geometry and apparent coupling varying along the strike of the trench axis. In the following sections, we first illustrate the surface velocity profiles in the presence and absence of slip-transition zones. We then consider the sensitivity of the surface observables determined from these velocity profiles – the hingeline, x_{hinge}, and location of maximum uplift rate, $x_{\max}$ – to the megathrust interface geometry as well as the assumed slip distribution.

3. Surface velocities predicted by EDMs

In this section, we discuss the surface velocities predicted by the BSM and the ESPM for a realistic megathrust interface profile, both with and without slip-transition zones. The formal sensitivity analysis for planar as well as curved faults is discussed in the following section. Fig. 1 schematically illustrates a typical profile of the vertical interseismic surface uplift-rate along a trench perpendicular transect across the megathrust interface for a locked zone of length s_{lock}, without a surrounding slip-transition zone. The surface observables, x_{hinge} and $x_{\max}$, are schematically located relative to the extent of the locked zone on the megathrust interface. As noted previously, $x_{\max}$ for the interseismic period corresponds to location of maximum subsidence, x_{min}, during the coseismic and early post-seismic period. Notable

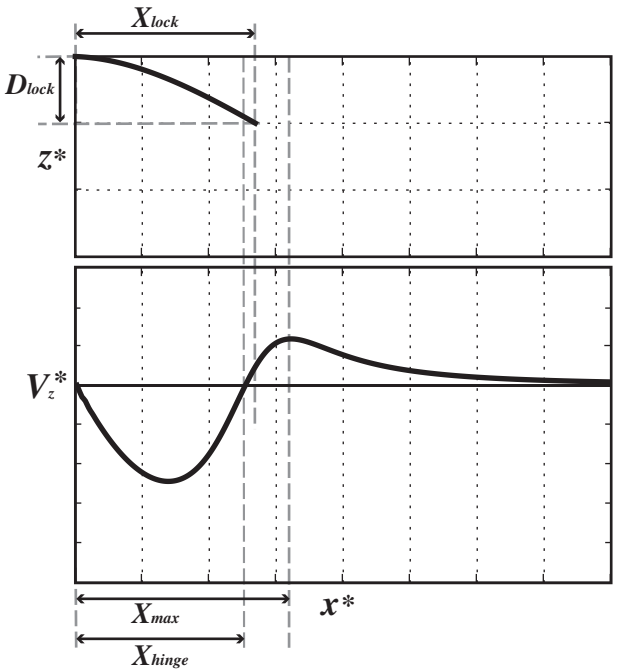

Fig. 1. Schematic illustration showing the relative locations of surface observables, x_{hinge}, x_{lock}, and x_{max}, using a typical vertical velocity profile from slip on a locked patch located along a curved fault.

features of the surface displacement rates predicted for locked asperities without slip-transition zones include (see black profiles in the middle and bottom panels of Fig. 2a–d): (i) maximum strain-rates above the region of highest curvature of the fault profile; (ii) zero strain-rates, and peak uplift rates, roughly above the downdip end of the locked asperity; and (iii) low horizontal strain-rates in the vicinity of the trench.

For intuition building purposes, we first discuss the effect of kinks and curvature (i.e., non-planar locked zones) on surface velocity predictions (Fig. 3). We start with a locked patch along a curved fault interface and approximate it with two planar segments intersecting at a kink. We compare surface velocity profiles predicted by the resulting kinked fault when these two segments intersect successively deeper along the curved fault interface (i.e., the kink moves closer to the bottom of the locked patch). We also choose three different planar fault approximations to the kinked fault: (i) fault-*s*: a shallow fault coinciding with the upper segment of the kink, but having the same overall extent of locking, s_{lock}, as the kinked fault, (ii) fault-*d*: a fault tangential to the downdip end of the locked patch — i.e. parallel to the lower segment of the kinked fault, and having the same D_{lock}, that intersects the free-surface landward of the trench, and (iii) fault-*m*: a fault patch with its top and bottom edges coinciding with the trench and D_{lock}, respectively, so its slope is the same as the mean slope of the two kink segments.

At distances beyond $2D_{lock}$ landward from the trench, the surface velocity profile due to locking along a curved interface (fault-*F*, Fig. 3a) can be approximated by locking along a planar fault tangential to that interface near the bottom of the locked zone (fault-*d*, Fig. 3a; see Kanda and Simons (2010) for a more extensive discussion). If we approximate this curved fault by a kinked fault with two planar segments of roughly equal size, (fault-*F*, Fig. 3b), we find that the latter's surface velocity predictions are very similar to those for the curved fault at distances beyond $2D_{lock}$ from the trench. At these distances, the velocity profiles predicted by both faults (including surface observables, x_{hinge} and $x_{\max}$) are identical because fault-*d* directly overlaps with the lower segment of fault-*F* (Fig. 3b). Also because of its partial overlap with fault-*F*, fault-*s* also matches the former's predictions, but only in the far field ($>4D_{lock}$ from the trench, Fig. 3b). The large strain-rates directly beneath the kink

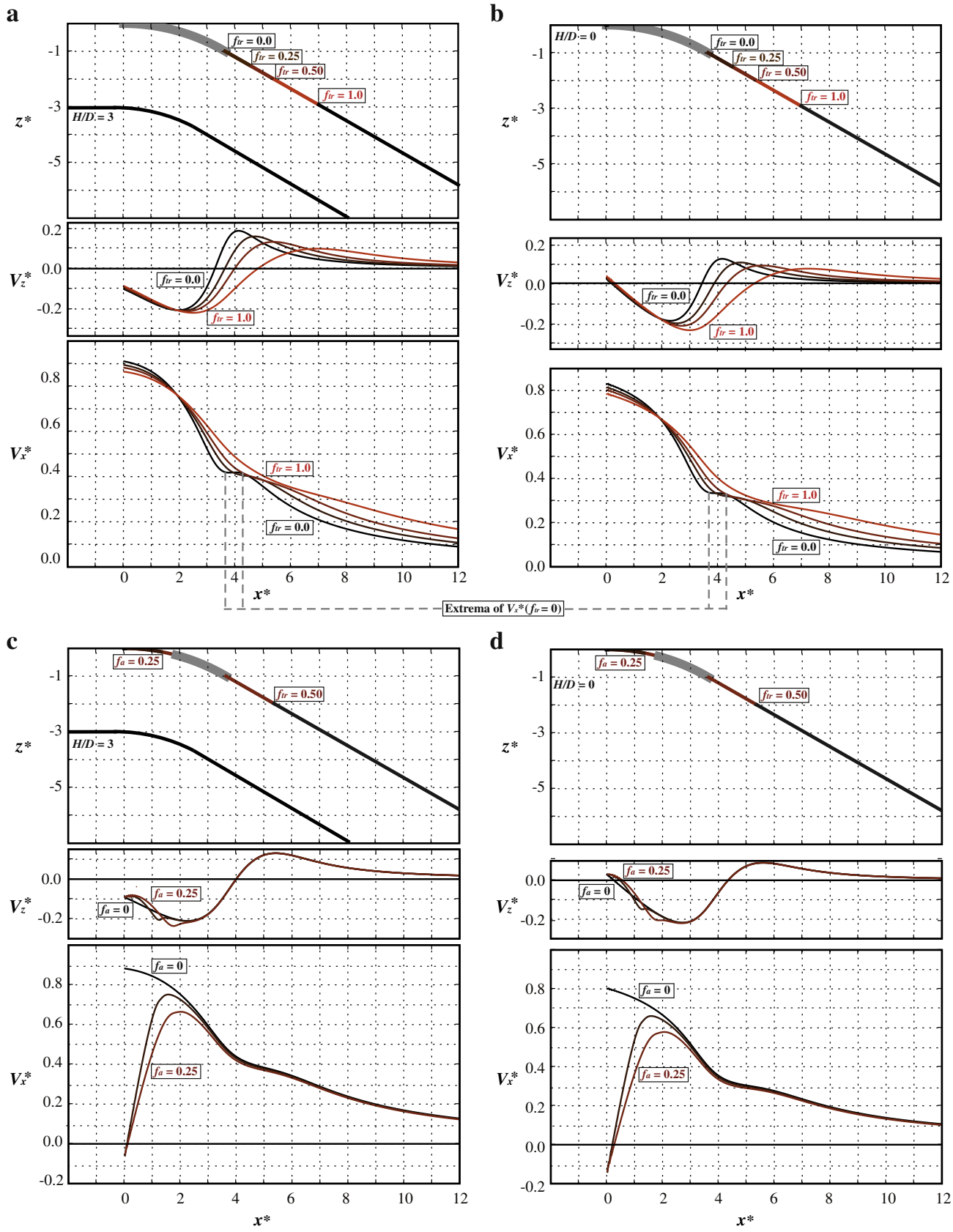

Fig. 2. Effect of doubling the width of the transition zones updip and downdip of the locked megathrust interface for the ESPM (shown for a slab thickness to locking depth ratio, H/D = 3) and the BSM. f_{tr} (f_a) is the fractional length of the downdip (updip) transition zone relative to the width of the locked megathrust, s_{tr}/s_{lock} (s_a/s_{lock}). (a, b) Downdip transition zones: results are presented for $f_{tr} = 0$, 0.25, 0.5, and 1. (c, d) Updip transition zones: results are presented for $f_a = 0$, 0.125, and 0.25. Axes are as described in text.

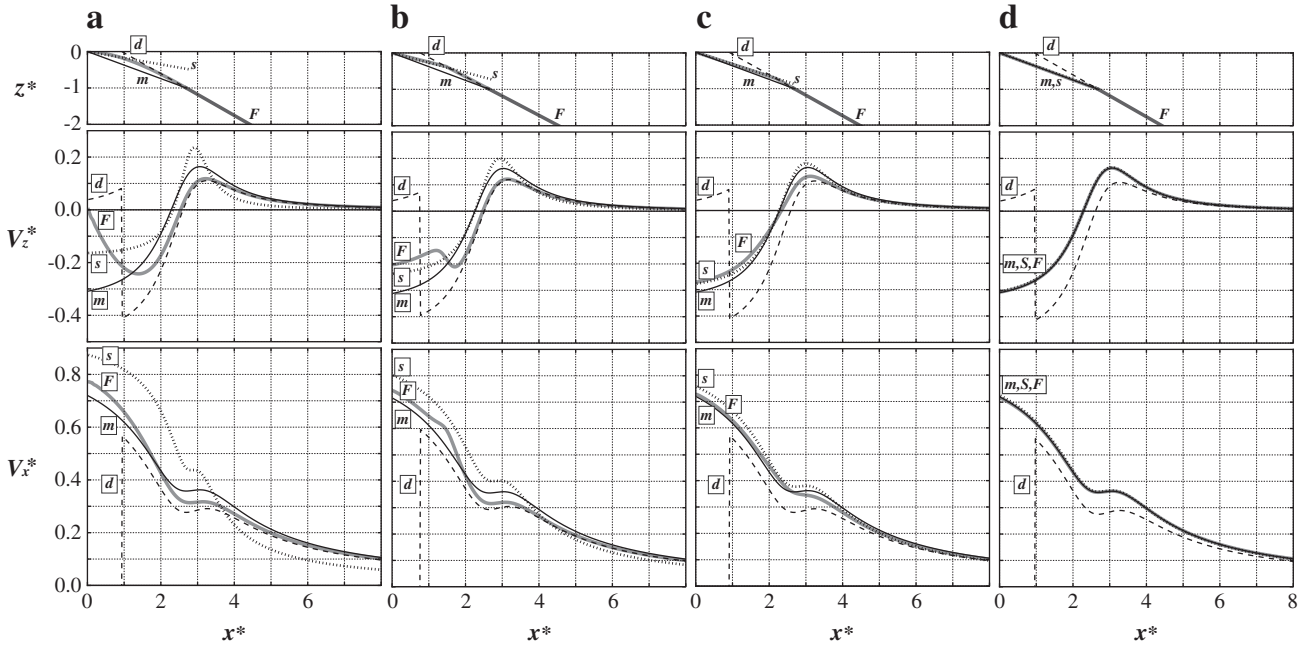

Fig. 3. Approximation of a realistic, curved fault with a kinked fault interface. The kinked fault (fault-F, thick gray line) is derived from the two end-member planar faults: fault-s (dotted line) representing a planar fault identical to the upper segment of the kink, and having the same locking extent of the entire kinked fault; and fault-d (dashed line) representing a planar fault identical to the lower segment of the kink and having the same locking depth. Fault-m represents a fault having the same end-points for its locked patch as fault-F, but with a slope equal to the mean for the two kink segments. Panels shown represent fault cross-sections (top), and velocity profiles — vertical (middle), horizontal (bottom). (a) Curved fault (thick gray line, fault-F) with locking depth, D_{lock}; and its kinked fault approximations (thick gray lines, fault-F) with the kink located at a depth of: (b) 0.5 D_{lock}, (c) 0.75 D_{lock}, and (d) D_{lock}. Axes are as described in the text.

(represented by large slopes of the thick gray curves in the bottom two panels of Fig. 3b) are highly localized and do not propagate farther landward. Approximating the curved fault by another set of planar faults so that the kink is located deeper and closer to the bottom of the locked patch, we find that fault-*s* and fault-*m* approximate the surface observables for fault-*F* exceedingly well (Fig. 3c), even though none of the planar faults fit the surface velocity profiles of the kinked fault particularly well except in the far-field ($>4D_{lock}$ from the trench). Fault-*m* is the best overall estimator for the surface velocity profile of fault-*F* in this case. In the limiting case of a kink at the bottom of the locked interface (Fig. 3d), fault-*m* and fault-*s* are identical to the locked patch, and predict identical velocity profiles to fault-*F*. In summary, surface observables for kinked faults can be almost exactly estimated from those for the equivalent planar faults using: (a) fault-*d*, if the kink is shallower than $D_{lock}/2$, or (b) fault-*m* (or fault-*s*), if the kink lies between $D_{lock}/2$ and D_{lock}. Therefore we do not present a separate analysis for kinked faults here.

Our discussion so far considered locked patches across which slip transitions abruptly to zero. However, it is physically implausible for an abrupt transition from locked to creeping at the edges of a rupture asperity, as a simple EDM such as the above would imply. Stress concentrations would be too high for the material to behave elastically (e.g., Scholz, 1990). Simulations incorporating a frictional fault (rate-strengthening, or conditionally stable) between fully elastic hanging- and foot-walls suggest that such high stress concentrations result in the formation of a diffuse 'stress-shadow' region surrounding the locked zone due to high afterslip-rates early in the seismic cycle (e.g., Hetland and Simons, 2010). Recent studies also seem to infer that regions surrounding coseismic ruptures (i.e., asperities and afterslip/post-seismic-slip zones) experience significant slip relatively early in the seismic cycle (e.g., Biggs et al., 2007; Chen et al., 2009; Hsu et al., 2006; Miyazaki et al., 2004; Perfettini et al., 2010). However, a large multi-asperity earthquake can still rupture these stress-shadow regions around constituent asperities, as illustrated by the 2011, M9 Tohoku-oki earthquake. Therefore, the downdip limit of seismic activity along the megathrust interface may extend deeper than an individual rupture. This downdip limit is thought to be thermally controlled (Hyndman and Wang, 1993) and experience time-dependent inelastic deformation. The width of such a thermal transition zone depends on the fault rheology, and is thought to correspond to the 350° and 450° isotherms (Hyndman and Wang, 1993). Therefore, the location of the transition zone along the subduction interface strongly depends on both the geometry as well as local thermal structure.

The presence of an updip slip-transition zone may be harder to defend. For a subducting plate having a finite thickness, as represented in the ESPM (Kanda and Simons, 2010), the steady motion of its bottom surface can result in interseismic slip along the shallow portion of the plate interface (at velocities less than or equal to the plate convergence rate between the trench and depths of 5–10 km). Such shallow slip would be a proxy for the shear strain transmitted by the subducting plate to the frontal wedge, which is typically made up of unconsolidated sediments that do not have significant internal or basal strength. However, if the wedge were strong enough to support a conditionally stable megathrust interface (so elastic energy can be stored at the interface over the seismic cycle), then this entire shallow region updip of the asperity may be locked late in the seismic cycle. In fact, recent simulations of slip evolution on megathrust surfaces predict that such slip early in the seismic cycle can generate significant stress-shadow zones updip of seismic asperities, depending on the chosen fault rheology as well as asperity depth (Hetland and Simons, 2010). That there was significant shallow slip during the 2011, M9 Tohoku-oki (Japan) earthquake (e.g., Simons et al., 2011, Fig. S10) seems to agree with the above predictions of an updip stress-shadow region — implying that it may be more appropriate to assume that late in the seismic cycle, the zone of apparent locking can in places extend all the way to the trench (e.g., Wang et al., 2003). Nevertheless, in this section, we present the surface velocity profiles for an updip slip-transition zone because some modeling studies (e.g., using campaign-GPS or coastal uplift/subsidence data) invoke such a transition zone for explaining horizontal geodetic data close to the trench (e.g., Natawidjaja, 2003; Sieh et al., 1999; Subarya et al., 2006). Such a shallow slip-transition zone may be a proxy for

a stress-shadow zone over the conditionally stable megathrust interface updip of a seismic rupture.

As noted above, we approximate the above interseismic stress-shadow 'aprons' around seismic asperities by a transition zone having a monotonically decreasing slip deficit rate (as well as cumulative slip) away from the asperity. Thus, a trench-perpendicular transect across the center of such an asperity would show a locked zone experiencing the full slip-deficit rate (i.e., equal to the plate convergence rate), surrounded by updip and downdip 'transition-zones' where this rate tapers linearly to zero. Here, we consider both the ESPM (of plate thickness, H) and the BSM having (i) a lower transition zone of width, s_{tr}, along the plate interface downdip of the locked zone (or asperity), and (ii) a shallow transition zone of width, s_a, along the plate interface between the trench and the updip limit of the locked zone (Fig. 2, where the fractional transition zone widths are: $f_{tr}=s_{tr}/s_{lock}=[0, 0.25, 0.5, 1]$, and $f_a=s_a/s_{lock}=[0, 0.125, 0.25]$, are illustrated in shades of red). For comparison, Wang et al. (2003) assumed a transition zone whose width is as large as the locked zone for the Cascadia subduction zone. Along a downdip transition zone, we model slip-rate during the interseismic period as linearly increasing from zero at the lower edge of the asperity to the long-term plate convergence rate, V_P, farther downdip. Such a tapered slip zone is only partially slipping (creeping) during the interseismic period, but also slips during the coseismic and postseismic periods. Along the updip transition zone, we model interseismic slip-rate as linearly decreasing from a finite value (V_P) at the free surface, to zero just updip of the asperity.

A downdip transition zone with tapered slip - representing a conditionally stable region downdip of the asperity that is susceptible to future ruptures - increases the effective s_{lock} of the ESPM or the BSM. Therefore, the surface velocity profiles from dislocation models with a transition zone show deformation occurring over a broader region (or longer wavelength) than those for models having no transition zone (Fig. 2a,b). As a result, the slopes of both the vertical and horizontal velocity profiles (i.e., surface strain-rates) are shallower landward of x_{lock}, compared to those for models without a transition zone. Also, the local extremum (when $f_{tr}=0$), or flattening (when $f_{tr}>0$), in the horizontal velocity profiles (bottom panels, Fig. 2a,b) – roughly above the downdip end of the apparent locked zone – is located farther from the trench, and entirely disappears as the transition zone width increases (for $f_{tr}\geq 0.5$ here). So, using strain-rates (slopes of the velocity profiles) to locate the extent of the locked zone is not robust. More complex models have been invoked in interpreting such shallow slopes and broader wavelength deformation observed in horizontal velocities landward of x_{lock} (e.g., Williams and McCaffrey, 2001). Thus, vertical velocities (displacements) at the surface are more diagnostic of the extent of x_{lock} during the interseismic (coseismic + postseismic), compared to the horizontals. In addition, verticals are also less prone to reference errors, providing more robust constraints on model parameters (e.g., Aoki and Scholz, 2003; Métois et al., 2012).

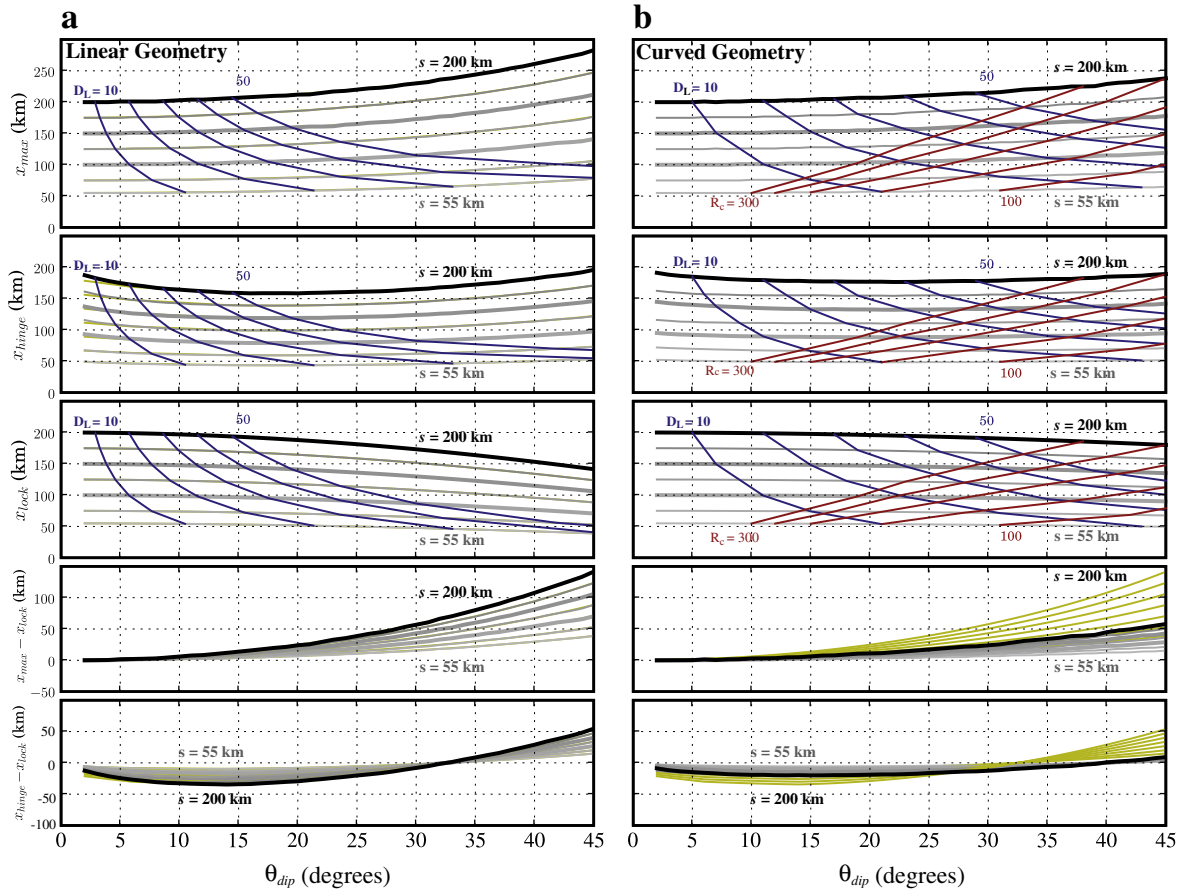

Fig. 4. Location of the maximum vertical velocity (x_{max}), zero vertical velocity (x_{hinge}), the surface projection of the bottom of locked fault (x_{lock}), and the differences between them, as a function of the length of the locked fault patch, s (= s_{lock} for both planar and curved faults; see Section 2), and dip angle at the bottom of s, θ. Each parameter is plotted for along-dip extents of the locked zone, s = 55, 75, 100, 125, 150, and 200 km. Thicker curves represent fault lengths of 100, 150, and 200 km. (a) Planar faults: blue curves (cutting across the s-curves from the top left to bottom right) are lines of constant locking depth (10 to 50 km, in steps of 10 km). Theoretical estimates for planar faults (see Section 4) are presented in dark yellow, but are almost exactly overlaid by the gray planar fault solutions calculated using our numerical code for arbitrary fault geometries. (b) Curved faults: red curves (cutting across the s-curves from the bottom right to top left) are lines of constant radii of curvature (100 to 300 km, in steps of 50 km). Blue curves are the same as in (a). Theoretical estimates for planar faults are also presented in the bottom two panels (yellow curves) for comparison.

Table 1
Theoretical estimates for the horizontal distance between the trench and the surface projection of the downdip end of the locked patch, x_{lock}, for planar and curved faults locked up to the trench. Planar, circular, and parabolic refer to geometric approximations of the megathrust cross-section. Dips for curved faults correspond to the slopes of their mean tangent planes between the seismogenic depth and 100 km.

Fault type	Dip range	Uncertainty in X_{lock} location
Planar fault	0°–27°	(0.9–1.1) $\bar{X}$[a]
	27°–50°	(0.9–1.6) X_{hinge}
Curved fault (circular/parabolic)	0°–37°	(0.95–1.05) $\bar{X}$[a]
	37°–50°	(0.95–1.1) X_{hinge}

[a] $\bar{X} = \left(\frac{X_{hinge}+X_{max}}{2}\right)$.

Table 2
Theoretical estimates for the horizontal distance between the trench and the surface projection of the downdip end of the locked patch, x_{lock}, for planar and curved faults having a transition in apparent coupling downdip of the locked zone. The results here are for a transition zone width of 25% of the length of the locked zone, s_{lock}. Dips for curved faults correspond to the slopes of their mean tangent planes between the seismogenic depth and 100 km.

Fault type	Dip range	Uncertainty in X_{lock} location
Planar fault	0°–25°	(0.9–1.1) x_{max}
	25°–32°	(0.95–1.1) $\bar{X}$[a]
	32°–50°	(0.9–1.4) X_{hinge}
Curved fault (circular/parabolic)	0°–27°	(0.93–1.03) x_{max}
	27°–35°	(0.95–1.0) $\bar{X}$[a]
	35°–50°	(0.9–1.1) X_{hinge}

[a] $\bar{X} = \left(\frac{X_{hinge}+X_{max}}{2}\right)$.

An updip transition zone, s_a, does not significantly affect the vertical surface velocity profiles predicted by either the ESPM or the BSM, at typical distances landward of the trench where most GPS stations are located (Fig. 2c,d). This insensitivity to s_a results from the shallow dip typical of most plate interfaces near the trench, which causes surface velocity perturbations (and strain-rates) to localize directly above the downdip end of these transition zones. This localization due to the shallow dip of curved faults near the trench is illustrated by the short wavelength (large strain-rate) character of velocity profiles for fault-s (dotted curves) in Fig. 3a. This localization of strain-rates near the trench is more marked in the horizontal velocities (bottom panels of Fig. 2c,d), where the velocities landward of x_{lock} are clearly not affected significantly by s_a. As noted above, such strong gradients in the horizontals have been observed where geodetic data are available closer to the trench (e.g., Sumatra: Natawidjaja, 2003; Sieh et al., 1999; Subarya et al., 2006), perhaps indicating ongoing updip postseismic slip – or frictionally stable rheology – updip of the locked zone.

The ESPM and the BSM surface velocity profiles are equally sensitive to a change in s_{tr} (assuming identical geometry and long-term plate convergence velocity; Fig. 2a,b). However, owing to the strong sensitivity of verticals to the effective plate thickness, in addition to s_{tr}, such profiles can still discriminate between the ESPM and the BSM. Therefore, for a given subduction interface geometry, vertical surface velocities are the key to not only differentiating between the ESPM and the BSM (i.e., whether geodetic data require a finite effective elastic plate thickness), but also the location of the effective x_{lock}. In addition, for most subduction zones or thrust faults (typically dipping at angles<40° at depths shallower than 100 km), surface horizontal velocities are much larger than the vertical velocities, and therefore have a much better signal-to-noise ratio. However, while uncertainties in the observed horizontal velocities are smaller than those for the verticals (sometimes by at least a factor of two), they are more susceptible to reference frame errors. If the BSM were used to fit interseismic geodetic data at a subduction zone where plate-bending is important (thick lithosphere, or large curvature), we would expect that the best-fit BSM will underestimate θ (or overestimate s_{lock}), in order to fit the longer wavelength profile predicted by the ESPM (Kanda and Simons, 2010).

4. Sensitivity of EDM predictions to fault geometry and transition zone extents

The cross-sectional geometry of the plate interface has a first order effect on the surface velocity predictions of EDMs, because of their strong dependence on the dip as well as depth of the dislocation below the free surface. In view of the wide applicability of the BSM, it is important to understand the sensitivity of surface observables (x_{hinge} and x_{max}) to parameterization of the BSM, especially interface geometry. Besides, field geologic studies of seismic cycle deformation frequently assume that the location of the hinge-line or pivot-line coincides with the downdip extent of coseismic rupture (i.e., $x_{hinge} \approx x_{lock}$, e.g., Meltzner et al. (2006), Natawidjaja (2003), Subarya et al. (2006), Taylor et al. (2008)). We explore the sensitivity of these surface observables to fault geometry — specifically, we quantify how the relative distance between x_{lock} and x_{hinge} or x_{max} (as well as the average of these distances) varies with fault dip, θ, for generalized fault geometries.

We start with the analytical expression for the surface vertical uplift rate due to an edge-dislocation in a half-space, normalized by the geologic plate convergence rate, V_p, v_z^*, as a function of trench perpendicular distance, x, dip, θ, and downdip extent of locked fault, s (corrected version of Freund and Barnett (1976) — see Savage (1983), and Rani and Singh (1992)):

$$v_z^* = \frac{v_z}{V_p} = \frac{\sin(\theta)}{\pi}\left[\left(\frac{xs.\sin(\theta)}{x^2+s^2-2xs.\cos(\theta)}\right) + \tan^{-1}\left(\frac{x-s.\cos(\theta)}{s.\sin(\theta)}\right) - \frac{\pi}{2}\right]. \quad (1)$$

To find the hinge-line location, x_{hinge}, we set the above equation to zero, and solve the resulting transcendental equation numerically using a non-linear root finding algorithm. Although not obvious from the above equation, for nearly vertical faults (as θ tends to 90°), x_{hinge} tends to infinity, and as θ tends to 0°, x_{hinge} tends to a value close to (but less than) s. As Savage (1983) showed, the location of the peak uplift rate obtained by differentiating Eq. (1), is

$$x_{max} = \frac{s}{\cos(\theta)}. \quad (2)$$

For nearly vertical faults, (as θ tends to 90°), x_{max} tends to infinity (but at a faster rate than x_{hinge}) and as θ tends to 0°, x_{max} tends to s. As discussed previously, the depth of locking, D_{lock}, for planar faults equals $s \cdot \sin(\theta)$, and the surface projection of the bottom of their locked zone is,

$$x_{lock} = s \cdot \cos(\theta). \quad (3)$$

Fig. 5. Dimensionless plots of the variation in the location of x_{max} and x_{hinge} as a function of fault dip in the BSM having a planar (a, c) or curved (b, d) plate interface geometry, with (c, d) or without (a, b) a transition zone (of fractional length, f_{tr} = 25%) downdip of the locked megathrust zone. Top panels: dimensionless relative distance between x_{max} and x_{lock} (Δx_m^*) as a function of the dip of the BSM fault; middle panels: dimensionless relative distances between x_{hinge} and x_{lock} (Δx_h^*); bottom panels: mean value of plots in top two panels. Theoretical estimates for planar faults without any transition zone (thick gray lines from part (a)) are repeated for each panel of (b), (c) and (d) for comparison. All ordinates are dimensionless, and expressed as positive and/or negative percentages of x_{lock}. Also shown in (b, d) are inferred megathrust interface dips near the bottom of the seismogenic zone for some of the major subducting plates around the world (in 5°-bins, compiled from various sources — see text for details).

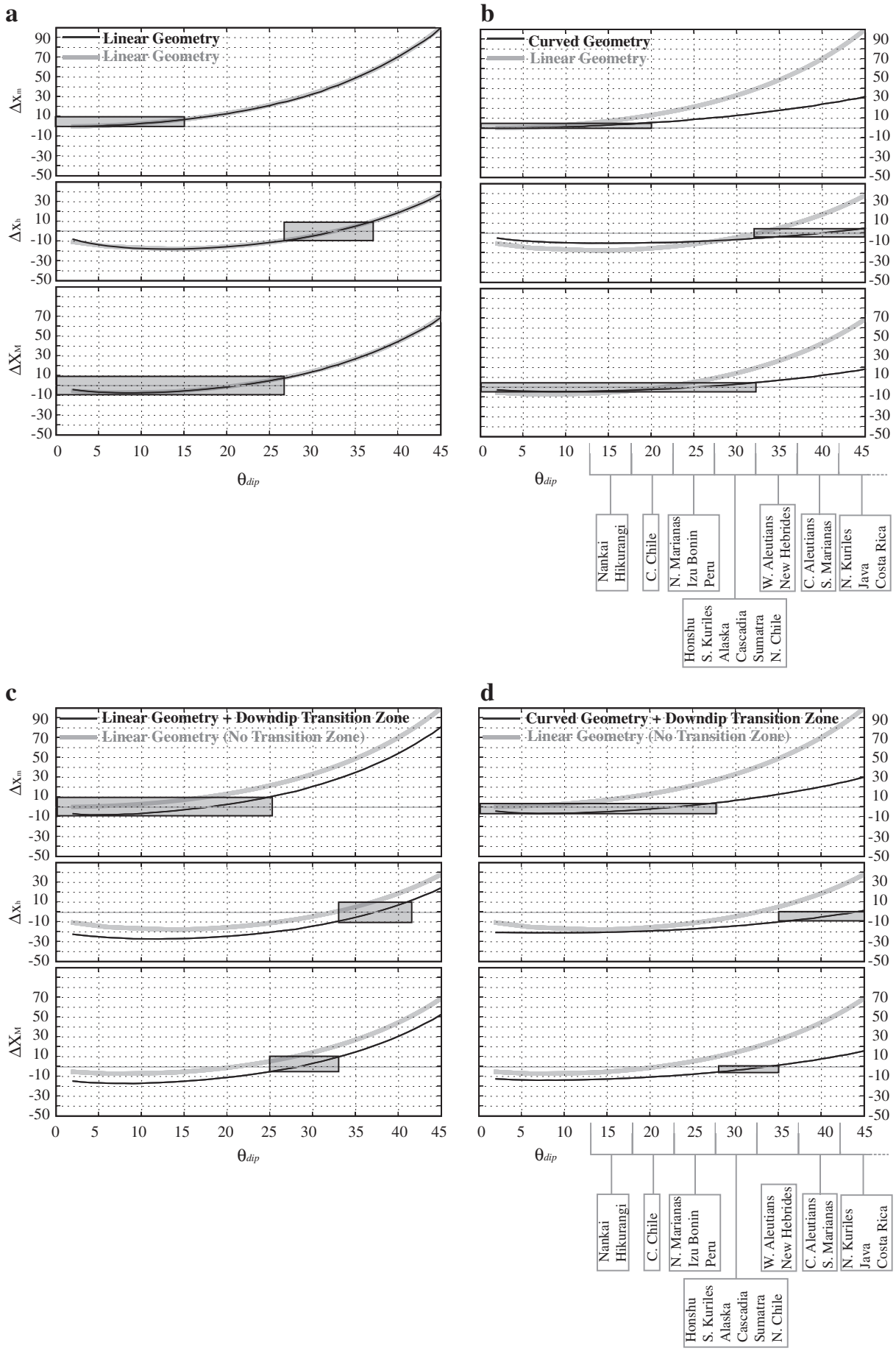
a
Linear Geometry
Linear Geometry
ΔXm
ΔXh
ΔXM
θdip
b
Curved Geometry
Linear Geometry
θdip
Nankai
Hikurangi
C. Chile
N. Marianas
Izu Bonin
Peru
W. Aleutians
New Hebrides
C. Aleutians
S. Marianas
N. Kuriles
Java
Costa Rica
Honshu
S. Kuriles
Alaska
Cascadia
Sumatra
N. Chile
c
Linear Geometry + Downdip Transition Zone
Linear Geometry (No Transition Zone)
ΔXm
ΔXh
ΔXM
θdip
d
Curved Geometry + Downdip Transition Zone
Linear Geometry (No Transition Zone)
θdip
Nankai
Hikurangi
C. Chile
N. Marianas
Izu Bonin
Peru
W. Aleutians
New Hebrides
C. Aleutians
S. Marianas
N. Kuriles
Java
Costa Rica
Honshu
S. Kuriles
Alaska
Cascadia
Sumatra
N. Chile

For nearly vertical faults (θ tending to 90°), x_{lock} tends to zero, but at a much slower rate than the rapid increase of either $x_{\max}$ or x_{hinge}; as θ tends to 0°, x_{lock} tends to s. For the analysis here, we choose as our independent parameters — the downdip extent of locked fault, s, and fault dip, θ, which naturally fall out of the analytical solution (Eq. (1)). Surface observables for planar faults (from the last three equations) are plotted in Fig. 4a (in yellow, but are exactly overlaid by the corresponding numerical solutions as discussed below). For curved faults, faults with downdip transition zones, as well as the ESPM, we first compute the vertical surface velocity field (v_z), for every combination of θ and s, at a resolution of 0.5°×50 km. We numerically compute the locations of both the hinge-line ($v_z = 0$) and maximum vertical uplift rate ($v_z' = 0$) — the results for curved faults are displayed in Fig. 4b. As a verification of our numerical procedure, notice that the yellow theoretical solutions for planar faults are not visible because they are exactly overlaid by the gray (numerical) solutions (Fig. 4a, all five panels). These same theoretical planar fault solutions are also plotted in the bottom two panels of Fig. 4b (yellow curves) for comparison with curved fault solutions.

We approximate the shallow dip typical of most megathrust interfaces near the trench by assigning zero dip to the curved fault profiles used here, at their intersection with the free surface (i.e., the 'trench'). Irrespective of fault geometry, x_{lock} monotonically decreases, and $x_{\max}$ monotonically increases with increasing dip at the bottom of the locked megathrust (s_{lock}, the distance from the trench to the bottom of the seismic asperity along the fault interface). However, x_{hinge} first decreases, then increases with dip. Such concave upward dependence with increasing dip implies that the hinge-line location changes from being trenchward of x_{lock} to landward of it (by 10–20% of s_{lock}) depending on the megathrust interface geometry. Also, comparing Eqs. (2) and (3) for planar faults, $x_{\max} \geq x_{lock}$ always (Fig. 4a) – a relationship that also holds for curved faults in general (Fig. 4b). The ratio, $x_{hinge}/x_{\max}$, varies between 70 and 90% for a wide range of megathrust interface dips, irrespective of both the geometry as well as the presence of a transition zone. The sensitivity of surface observables to uncertainties in dip at the bottom of the locked zone is weaker for curved megathrust geometries compared to the planar case — clearly illustrated by the relationships of peak uplift and hingeline locations relative to x_{lock} (yellow and black/gray suite of curves, bottom panels of Fig. 4b). As a result, the loci of constant locking depths for curved faults (blue curves, Fig. 4b) span a wider range of dips compared to those for planar faults (blue curves, Fig. 4a). For curved faults typical of most subduction zones ($\theta \leq 35°$), we found that the location of the surface observables do not differ significantly between geometries having constant or varying curvature (i.e., circular vs. parabolic approximations of the megathrust interface). So, we do not show separate graphical results for varying curvature, but instead encapsulate the main results in Tables 1 and 2. Henceforth, 'curved' is used synonymously with constant curvature approximations of the megathrust. For typical curved megathrust interfaces ($\theta \leq 35°$), decreasing radius of curvature results in a steeper dip near the bottom of the locked zone, affecting D_{lock} much more than x_{lock} or the other surface observables (red curves in Fig. 4b). That is, D_{lock} is much more sensitive to the actual megathrust geometry than x_{lock}.

Taking advantage of the proportionality of surface observables x_{hinge}, x_{lock}, and $x_{\max}$ to the downdip extent of locking, s_{lock} – either explicitly for planar faults, or implicitly for our parameterization of curved faults (see Section 2 above) – we can divide the ordinates in Fig. 4 by x_{lock}, so that plots for different locking extents collapse into a single curve for either fault geometry (black curves, Fig. 5). We now illustrate the dependence of the BSM's x_{hinge} and $x_{\max}$ as on the dip, θ, and arc-length, s_{lock}, for planar faults without a downdip transition zone (Fig. 5a), curved faults without a downdip transition zone (Fig. 5b), planar faults having a downdip transition zone (Fig. 5c), and curved faults having a downdip transition zone (Fig. 5d). We do not consider updip transition zones further because of their negligible effect on the locations of our chosen surface observables (Section 3, and Fig. 2c–d). Within each part of Fig. 5, the top panel presents the relative dimensionless distance between $x_{\max}$ and x_{lock},

$$\Delta x_m = (x_{\max} - x_{lock})/x_{lock}. \quad (4)$$

The middle panel presents the relative dimensionless distance between x_{hinge} and x_{lock},

$$\Delta x_h = \left(x_{hinge} - x_{lock}\right)/x_{lock}. \quad (5)$$

The bottom panel presents the relative distance of the mean of x_{hinge} and $x_{\max}$, from x_{lock} — i.e., mean of Eqs. (4) and (5), $\Delta X_M = (\Delta x_m + \Delta x_h)/2 = [(x_{hinge} + x_{\max})/2 - x_{lock}]/x_{lock}$.

For the BSM, ranges of dip within which x_{hinge}, $x_{\max}$, or some combination of the two is a 'good predictor' of the location of x_{lock} (i.e., with uncertainty $\leq \pm 10\%$ of x_{lock}) are highlighted using gray boxes in Fig. 5 and encapsulated in Table 1 (for faults without any downdip transition zone) and Table 2 (for faults with a downdip transition zone, $f_{tr} = 25\%$). For the more realistic curved megathrusts (Fig. 5b,d), we also indicate major subduction zones around the world corresponding to each dip-range (compiled from Engdahl et al., 2007; Lallemand et al., 2005; Parsons et al., 1998; Syracuse and Abers, 2006). For the ESPM (not shown), we find that the variation of the above dimensionless parameters with dip angle is qualitatively similar to that for the corresponding BSM, but with larger uncertainties.

For shallow dips characteristic of most subduction zones ($\theta \leq 30°$ irrespective of geometry), x_{hinge} is located trenchward of x_{lock} (so, Δx_h is negative), while $x_{\max}$ lies landward of it (Δx_m is always positive), but almost equally distant — irrespective of the extent of s_{lock} (top and middle panels, Fig. 5a,b). We find that the mean of these two values, represented by ΔX_M, to be a good estimator of x_{lock} for shallow dipping interfaces (bottom panels, Fig. 5a,b) — to within $\pm 10\%$ for planar faults and only half that uncertainty, or $\pm 5\%$, for curved faults. For steeper dips ($30° < \theta \leq 50°$), both x_{hinge} and $x_{\max}$ lie on the same side of x_{lock}, with the former being much closer to it (Fig. 4). Therefore, x_{hinge} is a better estimator of x_{lock} compared to $x_{\max}$ only for such steep plate interfaces (middle panels, Fig. 5a,b). For shallow dipping interfaces, using x_{hinge} as a proxy for x_{lock} can result in significant underestimates of the extent of locking. For example, for s_{lock} of 200 km, the discrepancy between x_{hinge} and x_{lock} can be as high as 40 km. It is interesting to note that for planar faults without slip transition zones, x_{hinge} is the best estimator of x_{lock} for dips in the range of 27°–37° (middle panel, Fig. 5a). This range of dips includes some of the longest studied subduction zones — e.g., northern Japan (Honshu and S. Kuriles), Alaska, and Chile. So, the common notion that the hingeline coincides with the downdip extent of coseismic rupture (i.e., $x_{hinge} \approx x_{lock}$) may have originated from early studies of these subduction zones assuming planar megathrusts (e.g., Savage, 1983).

In the intuition-building toy models presented in Fig. 5c and d, we only consider a single transition zone width that is 25% of the extent of locked zone (equivalent to the $f_{tr} = 0.25$ case in Fig. 1a). The increase in effective extent of locking, s_{lock}, due to a downdip transition zone (of fractional width f_{tr}, Fig. 1a,b), along with our parameterization of x_{lock} in terms of the extent of locking, implies that the effective interseismic x_{lock} also increases roughly by a factor of f_{tr} irrespective of the fault geometry. Therefore, in the presence of a downdip transition zone, both Δx_h and Δx_m are negative for shallow dips (up to $\theta \sim 25°$–30°, Fig. 5c,d, top panels) — that is, x_{hinge} and $x_{\max}$ shift trenchward from their locations for the BSM without transition zones. Thus, in the presence of a downdip transition zone, $x_{\max}$ is closer to x_{lock} than x_{hinge}, and a better predictor for x_{lock} than any other surface observable (to within $\pm 10\%$ for planar faults, and $\pm 5\%$ for curved faults; top panels, Fig. 5c,d). We find that doubling f_{tr} roughly doubles the uncertainty in the location of x_{lock} using either Δx_m, or the mean,

ΔX_M (results not shown here) — in other words, the uncertainty boxes in Fig. 5c and d shift to the right towards steeper faults. Therefore, for larger transition zones, the notion that $x_{hinge} \sim x_{lock}$ may be significantly incorrect. Further, the uncertainty in locating x_{lock} accurately from any of the above surface observables becomes large for very shallow dipping fault interfaces ($\theta \leq 20°$).

The presence of a bottom plate surface in the ESPM shifts x_{hinge} trenchward (see, Kanda and Simons, 2010). For shallow dips ($\theta < 20°$), the effect of plate bending is small, and the dimensionless parameter curves x_{hinge} are nearly identical to those for the corresponding BSM plate interface geometry in Fig. 5. For steeper dips, x_{hinge} is located trenchward relative to that for the BSM having the same s_{lock} and θ. Therefore, the distance between x_{hinge} and x_{lock} will be negative over a wider range of θ, compared to the corresponding BSM. Also, $x_{\max}$ for the ESPM with a finite plate thickness changes little from its value for the ESPM having zero plate thickness (that is, the BSM) (Kanda and Simons, 2010). The above results were confirmed for the ESPM having planar or curved interface geometry and different plate thicknesses. In general, we find that x_{lock} for the ESPM can be constrained using the same dimensionless parameters as those for the BSM (Tables 1 and 2), for shallow dips ($<20°$). Even for the range, $20° < \theta < 30°$, the uncertainty in estimating x_{lock} using these tables is approximately only double that for the correspon-ding BSM. However, for steeper dips, the uncertainty in estimating x_{lock} from the above surface observables increases significantly for the ESPM, because of the strong effect of plate bending in that model, unless additional assumptions are made regarding how such bending stresses are accommodated (e.g., Kanda and Simons, 2010).

5. Conclusions

Here, we quantitatively compared the sensitivity of surface observables predicted by EDMs, x_{hinge} and $x_{\max}$, to: (i) variations in geometry of the megathrust interface, and (ii) tapered megathrust slip distribution late in the seismic cycle (i.e., during the interseismic period), expected due to postseismic slip over the region surrounding the seismic rupture zone ('asperity', or 'locked-zone') following the rupture. The results presented here for 2D "infinite" along-strike locked patches can be directly applied to realistic locked patches having finite widths unless such patches have aspect ratios less than 1, or are located along steeply dipping fault interfaces ($>45°$).

Predicted surface uplift rates and their gradients (i.e., surface shear strains corresponding to thrust slip, ε_{xz}) are much more sensitive to downdip transition zones than surface horizontal velocities (and corresponding horizontal compressive strains, ε_{xx}). Transition zones updip of seismic asperities impact horizontal velocities much more than verticals, because the typically shallower dips near the trench localize much of the strain there. However, much of the resulting stress accumulated updip of the seismic asperity is mostly dissipated by the interseismic period (e.g., Hetland and Simons, 2010), unless there is another asperity updip — e.g., the shallow asperity of the March, 2011, M_w 9 rupture off Tohoku, Japan (Tohoku-oki; e.g., Simons et al., 2011, Fig. S10), located updip from previously ruptured (and much smaller) asperities. Therefore, estimates of plate coupling are best constrained using both vertical uplift rates (which are most sensitive to the actual slip distribution), as well as horizontal velocities (which have high signal-to-noise ratio).

Surface observables such as x_{hinge} and $x_{\max}$ are significantly different for megathrusts with curved and planar fault cross-sections. Further, all surface observables for a fault having a downdip slope discontinuity (i.e., kinked fault) are well approximated by those for either its shallowest or deepest locked segment, depending on the depth of the kink. These observables are more sensitive to dip variations at, or near the downdip edges of seismogenic zones — especially for planar and kinked faults, in comparison to curved faults. Slip inversions should be carried out over as accurate a representation of the fault geometry as possible for a given subduction zone, in order to take advantage of this 'robustness' offered by megathrust interface curvature.

The common notion that the hingeline coincides with the downdip extent of coseismic rupture may originate from early studies of large subduction megathrust earthquakes in northern Japan, Alaska, and northern Chile, which were approximated to have occurred on planar faults dipping at ~30° (plate interface geometry in Fig. 2). For typical subduction zone geometries (curved megathrusts having a dip $\leq 30°$ at shallow depths, <100 km), and physically realistic, smooth slip-deficit distribution around seismic asperities, it is the location of the peak interseismic uplift rate, $x_{\max}$ (or the location of maximum coseismic subsidence) – rather than the location of the hinge-line, x_{hinge} – that provides a good approximation for the effective x_{lock}. For steeper faults, the mean of $x_{\max}$ and x_{hinge} provides a better approximation for the effective x_{lock}.

x_{hinge} approximates the location of x_{lock} only for the most steeply dipping megathrusts ($\theta \geq 45°$, e.g. Tonga-Kermadec) that have a narrow slip transition-zone. However, for such steeply dipping fault geometries, it is also important to consider the subducting plate thickness (i.e., the ESPM), or along-strike width of the locked patch. The difference between $x_{\max}$ and x_{hinge} can be significant for most realistic megathrust fault geometries, and can be as large as 50–100 km for realistic asperities experiencing significant afterslip. This large discrepancy when using x_{hinge} to locate x_{lock} will result in underestimating the seismic potential during the period immediately following rupture, and may also underestimate such potential during the interseismic (or preseismic) period. Therefore in addition to the hingeline, field based surveys of seismic hazard in subduction zones should also consider using the location of either the maximum coseismic subsidence, or the peak interseismic uplift-rate.

Notation

D, D_{lock}, D_L	Depth of locking along the fault/plate interface
d_a	Depth to bottom of updip transition zone, or to the updip limit of locked zone
F_{asp}	Asperity aspect ratio, $F_{asp} = W/s_{lock}$
f_{tr}	Fractional length of transition zone downdip of locked plate interface, s_{tr}/s_{lock}.
f_a	Fractional depth of updip transition zone w.r.t. locking depth, d_a/D_{lock}.
H	Thickness of the subducting plate in the ESPM
R, R_c	Local radius of curvature for the centerline of the plate
s	Arc-length along the plate interface, or along-dip distance over the locked asperity
s_{lock}	Along-dip extent of locked plate interface or asperity
s_a	Along-dip extent of the transition zone updip of the locked plate interface
s_{tr}	Along-dip extent of the transition zone downdip of the locked plate interface
V_x^*	Horizontal surface velocity, v_x, normalized by plate rate, v_x/V_p
V_z^*	Vertical surface velocity, v_z, normalized by plate rate, v_z/V_p
V_b, V_p	Backslip/plate-convergence velocity along the megathrust interface
W	Along-strike extent of locked plate interface or asperity
x	Horizontal coordinate, positive landward, or away from the trench
x^*	Horizontal coordinate, normalized w.r.t. locking depth, x/D_{lock}
x_{hinge}	Distance from the trench to the location of zero vertical surface velocity
x_{lock}	Distance between trench and surface projection of the downdip end of the locked zone
x_{max}	Distance from trench to the location of the peak in the vertical surface velocity field
z	Vertical coordinate, positive upward (depths are therefore, negative)

z^*	Vertical coordinate, normalized w.r.t. locking depth, z/D_{lock}
Δx_h	Dimensionless distance between x_{hinge} and x_{lock}, $(x_{hinge} - x_{lock})/x_{lock}$
Δx_m	Dimensionless distance between x_{max} and x_{lock}, $(x_{max} - x_{lock})/x_{lock}$
ΔX_M	Mean of dimensionless relative distances Δx_m and Δx_h: $(\Delta x_m + \Delta x_h)/2$
θ, θ_{dip}	Fault/plate interface dip (for a non-planar fault, this is measured at the bottom of the seismogenic zone)

Acknowledgments

We thank Yuri Fialko and Eric Hetland for insightful discussions. We also thank Charles Williams and an anonymous reviewer, whose constructive critiques helped improve the overall clarity of this paper. All plots in this paper were generated using Matplotlib, a Python based open-source package for 2D and 3D data visualization. This research was supported in part by the Gordon and Betty Moore Foundation. This is Caltech Tectonic Observatory Contribution #186, and Caltech Seismological Laboratory publication 10065.

References

Aoki, Y., Scholz, C.H., 2003. Vertical deformation of the Japanese islands, 1996–1999. Journal of Geophysical Research 108, 2257. http://dx.doi.org/10.1029/2002JB002129.

Biggs, J., Robinson, D.P., Dixon, T., 2007. The 2007 Pisco, Peru, earthquake (M8.0): seismology and geodesy. Geophysical Journal International 176, 657–669. http://dx.doi.org/10.1111/j.1365-246X.2008.03990.x.

Briggs, R.W., Sieh, K., Meltzner, A.J., Natawidjaja, D., Galetzka, J., Suwargadi, B., Hsu, Y.-j, Simons, M., Hananto, N., Suprihanto, I., Prayudi, D., Avouac, J.-P., Prawirodirdjo, L., Bock, Y., 2006. Deformation and slip along the Sunda megathrust in the Great 2005 Nias–Simeulue earthquake. Science 311. http://dx.doi.org/10.1126/science.1122602.

Chen, T., Newman, A.V., Feng, L., Fritz, H.M., 2009. Slip distribution from the 1 April 2007 Solomon Islands earthquake: a unique image of near-trench rupture. Geophysical Research Letters 36, L16307. http://dx.doi.org/10.1029/2009GL039496.

Cohen, S.C., 1999. Numerical models of crustal deformation in seismic zones. Advances in Geophysics 41, 133–231.

Delouis, B., Philip, H., Dorbath, L., Cisternas, A., 1998. Recent crustal deformation in the Antofagasta region (northern Chile) and the subduction process. Geophysical Journal International 132, 302–338.

Dorobek, S.L., 2008. Carbonate-platform facies in volcanic-arc settings: characteristics and controls on deposition and stratigraphic development. In: Draut, A.E., Clift, P.D., Scholl, D.W. (Eds.), Formation and Applications of the Sedimentary Record in Arc Collision Zones, pp. 55–90. http://dx.doi.org/10.1130/2008.2436(04).

Engdahl, E.R., Villasenor, A., DeShon, H.R., Thurber, C., 2007. Teleseismic relocation and assessment of seismicity (1918–2005) in the region of the 2004 Mw 9 Sumatra–Andaman and 2005 M 8.7 Nias great earthquakes. Bulletin of the Seismological Society of America 97, S43–S61.

Freund, L.B., Barnett, D.M., 1976. A two-dimensional analysis of surface deformation due to dip-slip faulting. Bulletin of the Seismological Society of America 66, 667–675.

Hetland, E.A., Simons, M., 2010. Postseismic and interseismic deformation due to fault creep II: transient creep and interseismic stress shadows on megathrusts. Geophysical Journal International 181, 99–112. http://dx.doi.org/10.1111/j.1365-246X.2009.04482.x.

Hsu, Y.-J., Simons, M., Avouac, J.-P., Galetzka, J., Sieh, K., Chlieh, M., Natawidjaja, D., Prawirodirdjo, L., Bock, Y., 2006. Frictional afterslip following the 2005 Nias–Simeulue earthquake, Sumatra. Science 312, 1921–1926.

Hsu, Y.-J., Simons, M., Williams, C., Casarotti, E., 2011. Three-dimensional FEM derived elastic Green's functions for the coseismic deformation of the 2005 Mw 8.7 Nias–Simeulue, Sumatra earthquake. Geochemistry, Geophysics, Geosystems 12, Q07013. http://dx.doi.org/10.1029/2011GC003553.

Hyndman, R.D., Wang, K., 1993. Thermal constraints on the zone of major thrust earthquake failure: the Cascadia subduction zone. Journal of Geophysical Research 98, 2039–2060.

Kanda, R.V.S., Simons, M., 2010. An elastic plate model for interseismic deformation in subduction zones. Journal of Geophysical Research 115, B03405.

Khazaradze, G., Klotz, J., 2003. Short and long-term effects of GPS measured crustal deformation rates along the South-Central Andes. Journal of Geophysical Research 108, 2289.

Koketsu, K., Hikima, K., Miyazaki, S., Ide, S., 2004. Joint inversion of strong motion and geodetic data for the source process of the 2003 Tokachi-oki, Hokkaido, earthquake. Earth Planets Space 56, 329–334.

Lallemand, S., Heuret, A., Boutelier, D., 2005. On the relationships between slab dip, back-arc stress, upper plate absolute motion and crustal nature in subduction zones. Geochemistry, Geophysics, Geosystems 6, Q09006. http://dx.doi.org/10.1029/2005GC000917.

Masterlark, T., DeMets, C., Wang, H.F., Sanchez, O., Stock, J., 2001. Homogeneous vs heterogeneous subduction zone models: coseismic and postseismic deformation. Geophysical Research Letters 28, 4047–4050. http://dx.doi.org/10.1029/2001GL013612.

Meltzner, A., Sieh, K., Abrams, M., Agnew, D.C., Hudnut, K.W., Avouac, J., Natawidjaja, D., 2006. Uplift and subsidence associated with the great Aceh–Andaman earthquake of 2004. Journal of Geophysical Research 111, B02407. http://dx.doi.org/10.1029/2005JB003891.

Métois, M., Socquet, A., Vigny, C., 2012. Interseismic coupling, segmentation and mechanical behavior of the central Chile subduction zone. Journal of Geophysical Research 117, B03406. http://dx.doi.org/10.1029/2011JB008736.

Miyazaki, S., Segall, P., Fukuda, J., Kato, T., 2004. Space time distribution of afterslip following the 2003 Tokachi-oki earthquake: implications for variations in fault zone frictional properties. Geophysical Research Letters L06623.

Natawidjaja, D.H., 2003. Neotectonics of the Sumatran fault and paleogeodesy of the Sumatran subduction zone. Ph.D. Thesis, California Institute of Technology, Pasadena, CA.

Okada, Y., 1992. Internal deformation due to shear and tensile faults in a half-space. Bulletin of the Seismological Society of America 82, 1018–1040.

Ortlieb, L., Barrientos, S., Guzman, N., 1996. Coseismic coastal uplift and coralline algae record in Northern Chile: the 1995 Antofagasta earthquake case. In: Scott, D.B., Ortlieb, L. (Eds.), Records of rapid events in late quaternary shorelines: Quaternary Science Reviews, pp. 949–960.

Parsons, T., Trehu, A.M., Luetgert, J.H., Miller, K., Kilbride, F., Wells, R.E., Fisher, M.A., Flueh, E., ten Brink, U.S., Christiansen, N.I., 1998. A new view into the Cascadia subduction zone and volcanic arc: implications for earthquake hazards along the Washington margin. Geology 26, 199–202.

Perfettini, H., Avouac, J., Tavera, H., Kositsky, A., Nocquet, J.-M., Bondoux, F., Chlieh, M., Sladen, A., Audin, L., Farber, D., Soler, P., 2010. Seismic and aseismic slip on the Central Peru megathrust. Nature 465, 78–81. http://dx.doi.org/10.1038/nature09062.

Rani, S., Singh, S.J., 1992. Static deformation of a uniform half-space due to a long dip-slip fault. Geophysical Journal International 109, 469–476.

Savage, J.C., 1983. A dislocation model of strain accumulation and release at a subduction zone. Journal of Geophysical Research 88, 4984–4996.

Savage, J.C., 1995. Interseismic uplift at the Nankai subduction zone, Southwest Japan, 1951–1990. Journal of Geophysical Research 100, 6339–6350.

Savage, J.C., 1998. Displacement field for an edge dislocation in a layered half-space. Journal of Geophysical Research 103, 2439–2446.

Scholz, C.H., 1990. The Mechanics of Earthquakes and Faulting. Cambridge University Press, New York.

Sieh, K., Ward, S.N., Natawidjaja, D., Suwargadi, B.W., 1999. Crustal deformation at the Sumatran subduction zone revealed by coral rings. Geophysical Research Letters 26, 3141–3144.

Simons, M., Minson, S.E., Sladen, A., Ortega, F., Jiang, J., Owen, S.E., Meng, L., Ampuero, J.-P., Wei, S., Chu, R., Helmberger, D.V., Kanamori, H., Hetland, E., Moore, A.W., Webb, F.H., 2011. The 2011 magnitude 9.0 Tohoku-Oki Earthquake: mosaicking the megathrust from seconds to centuries. Science. http://dx.doi.org/10.1126/science.1206731.

Sladen, A., Tavera, H., Simons, M., Avouac, J.P., Konca, A.O., Perfettini, H., Audin, L., Fielding, E.J., Ortega, F., Cavagnoud, R., 2009. Source model of the 2007 Mw 8.0 Pisco, Peru earthquake — implications for seismogenic behavior of subduction megathrusts. Journal of Geophysical Research 115. http://dx.doi.org/10.1029/2009JB006429.

Subarya, C., Chlieh, M., Prawirodirdjo, L., Avouac, J.P., Bock, Y., Sieh, K., Meltzner, A., Natawidjaja, D., McCaffrey, R., 2006. Plate-boundary deformation of the great Aceh–Andaman earthquake. Nature 440, 46–51.

Suwa, Y., Miura, S., Hasegawa, A., Sato, T., Tachibana, K., 2006. Interplate coupling beneath NE Japan inferred from three-dimensional displacement field. Journal of Geophysical Research 111, B04402.

Syracuse, E.M., Abers, G.A., 2006. Global compilation of variations in slab depth beneath arc volcanoes and implications. Geochemistry, Geophysics, Geosystems 7, Q05017. http://dx.doi.org/10.1029/2005GC001045.

Taylor, F.W., Briggs, R.W., Frohlich, C., Brown, A., Hornbach, M., Papabatu, A.K., Meltzner, A., Billy, D., 2008. Rupture across arc segment and plate boundaries in the 1 April 2007 Solomons earthquake. Nature Geoscience 1, 253–257.

Tomar, S., Dhiman, N.K., 2003. 2-D deformation analysis of a half-space due to a long dip-slip fault at finite depth. Proceedings of the Indian Academy of Sciences—Earth and Planetary Sciences 112, 587–596.

Vargas, G., Farías, M., Carretier, S., Tassara, A., Baize, S., Melnick, D., 2011. Coastal uplift and tsunami effects associated to the 2010 Mw 8.8 Maule earthquake in Central Chile. Andean Geology 38, 219–238.

Wang, K., Hu, Y., 2006. Accretionary prisms in subduction earthquake cycles: The theory of dynamic Coulomb wedge. Journal of Geophysical Research 111, B06410.

Wang, K., Wells, R., Mazzotti, S., Hyndman, R.D., Sagiya, T., 2003. A revised dislocation model of interseismic deformation of the Cascadia subduction zone. Journal of Geophysical Research 108, 2026.

Williams, C.A., McCaffrey, R., 2001. Stress rates in the central Cascadia subduction zone inferred from an elastic plate model. Geophysical Research Letters 28, 2125–2128.

Zweck, C., Freymueller, J.T., Cohen, S.C., 2002. Three-dimensional elastic dislocation modeling of the postseismic response to the 1964 Alaska earthquake. Journal of Geophysical Research 107, 2064.